24-2-2006

Spray pyrolyzed PbO-carbon nanocomposites as anode for lithium-ion batteries

S. H. Ng
University of Wollongong

J. Wang
University of Wollongong

Konstantin Konstantinov
University of Wollongong, konstan@uow.edu.au

D. Wexler
University of Wollongong, davidw@uow.edu.au

Jun Chen
University of Wollongong, junc@uow.edu.au

See next page for additional authors

Journal of The Electrochemical Society, **153** (4) A787-A793 (2006)
0013-4651/2006/153(4)/A787/7/$20.00 © The Electrochemical Society

Spray Pyrolyzed PbO-Carbon Nanocomposites as Anode for Lithium-Ion Batteries

S. H. Ng,[a,z] J. Wang,[a] K. Konstantinov,[b] D. Wexler,[c] J. Chen,[d,*] and H. K. Liu[a,*]

[a]*Institute for Superconducting and Electronic Materials and ARC Centre for Nanostructured Electromaterials, University of Wollongong, Wollongong, NSW 2522, Australia*
[b]*Institute for Superconducting and Electronic Materials, University of Wollongong, Wollongong, NSW 2522, Australia*
[c]*Faculty of Engineering, University of Wollongong, Wollongong, NSW 2522, Australia*
[d]*ARC Centre for Nanostructured Electromaterials and Intelligent Polymer Research Institute, University of Wollongong, Wollongong, NSW 2522, Australia*

A new approach has been used to prepare nanostructured lead oxide-carbon (PbO-C) composites via the spray pyrolysis technique. In this study, the electrochemical performance of the PbO-carbon nanocomposites as anode materials for lithium-ion rechargeable batteries was investigated. The prepared powders consist of fine nanocrystalline PbO homogeneously distributed within an amorphous carbon matrix with highly developed surface area. The estimated average crystal sizes of these nanocomposites from X-ray diffraction (XRD) patterns are in the range of 26–102 nm. The combination of spray technology and carbon addition increased the specific surface area (above 6 $m^2\ g^{-1}$) and the conductivity of PbO, improved the specific capacity, and maintained cycle life with a reversible capacity above 100 mAh g^{-1} beyond 50 cycles. The increase in capacity retention for PbO-carbon compared to that of pure PbO was due to the presence of a conductive and highly developed carbon matrix that can absorb large volume changes during the alloying/dealloying of lead with lithium over the 1.50 to 0.01 V potential range, which yields Li_xPb alloys ($0 < x < 4.5$).
 [DOI: 10.1149/1.2172570]

Manuscript received November 14, 2005; revised manuscript received December 22, 2005.
Available electronically February 24, 2006.

A new generation of lithium-ion rechargeable batteries was developed in the early 1990s with the introduction of Stalion lithium-ion cells by Fuji Photo Film Celltec,[1,2] whose anodes consisted of amorphous tin-based oxides instead of carbonaceous-based materials. It was reported that these electrodes have twice the theoretical gravimetric capacity and four times more theoretical volumetric capacity than carbon. This marvelous discovery has sparked intensive research on new materials that are capable of alloying with lithium such as Al, Sn, Pb, In, Bi, Cd, Ag, Mg, Zn, Si, and Sb,[3-6] which have been investigated in the past decade. These materials show satisfactory Li-ion transport properties as well as a good lithium packing density and electrochemical potential. However, a substantial change in specific volume of the electrode upon continuous charging/discharging leads to loss of electrical contact, and thus capacity loss as well as macroscopic dimensional problems within the cell structure. Several methods have been proposed to solve this volume expansion problem, mainly by reducing the metal particle size,[7,8] limitation of cycling depth with a very thin reaction layer,[9,10] or by construction of bonded electrodes using Li^+-conducting intermetallic phases[11,12] as binder materials for small particle size active Li alloys.

Despite the various methods available for the production of the ultrafine nanoparticles used in Li-ion batteries, it is highly desirable to apply simple and highly productive techniques to produce both the anode and cathode materials. Moreover, if possible, we should fabricate them in situ to avoid the complicated and expensive technological procedures that might be featured in some methods.[13] The spray pyrolysis method fully satisfies these requirements because it is versatile, inexpensive, industrially oriented, and can be operated over a large temperature range (100–1000°C).[9,10,13-15]

Studies by Martos et al.[15] using sprayed lead oxide powders as anode material in Li-ion batteries show that the specific capacity fades on cycling when bulk powders are used. Therefore, we suggest the addition of a carbon source (sucrose solution) to enhance the electric conductivity of PbO and also increase its specific capacity and cycle life. This concept has proven to be successful in other studies.[14,16,17]

Although there have been reports on the usage of sprayed PbO (Ref. 9 and 15) as an anode material in Li-ion batteries, there have been scarcely any studies reported on PbO-carbon anodes in Li-ion batteries. In this work, we produced both nanostructured PbO and nanocomposite PbO-carbon using an in situ spray pyrolysis approach and investigated their electrochemical performance as anode materials for Li-ion batteries.

Experimental

Materials synthesis.— Lead oxide powders were prepared using a 0.5 M aqueous solution of lead nitrate, $Pb(NO_3)_2$ (Aldrich Chemicals) as the precursor, while the composite materials were prepared by mixing the initial solutions with aqueous sucrose ($C_{12}H_{22}O_{11}$) solutions in weight ratios [$Pb(NO_3)_2$:sugar] of 100:0, 70:30, 40:60, 15:85 and 0:100, respectively. The materials were obtained in situ via spraying at 800°C using a flow rate of 3.14 mL min^{-1} in a vertical-type spray pyrolysis reactor. The reactions are as follows

$$Pb(NO_3)_2(aq) \xrightarrow{800°C} PbO + NO_2\uparrow + O_2\uparrow + H_2O\uparrow + \text{energy}\uparrow \quad [1]$$

$$C_{12}H_{22}O_{11}(aq) \xrightarrow{800°C} C + H_2O\uparrow + \text{energy}\uparrow \quad [2]$$

$$C_{12}H_{22}O_{11}(aq) + O_2 \xrightarrow{800°C} CO_2 + H_2O\uparrow + \text{energy}\uparrow \quad [3]$$

$$[Pb(NO_3)_2 + C_{12}H_{22}O_{11}](aq) \xrightarrow{800°C} PbO + C + NO_2\uparrow + O_2\uparrow + CO_2\uparrow + H_2O\uparrow + \text{energy}\uparrow \quad [4]$$

Composition and structure determination.— The sprayed powders were characterized by X-ray diffraction (XRD) using a Philips PW1730 diffractometer with Cu Kα radiation and graphite monochrometer. Powder morphologies were investigated using a JEOL JSM 6460A scanning electron microscope (SEM). Transmission electron microscopy (TEM) investigations were performed using a JEOL 2011 200 keV analytical electron microscope. TEM samples were prepared by deposition of ground particles onto lacy carbon support films. Specific surface areas of the nanostructured particles and nanocomposites of PbO were measured with a Quantachrome

* Electrochemical Society Active Member.
z E-mail: shn076@uow.edu.au

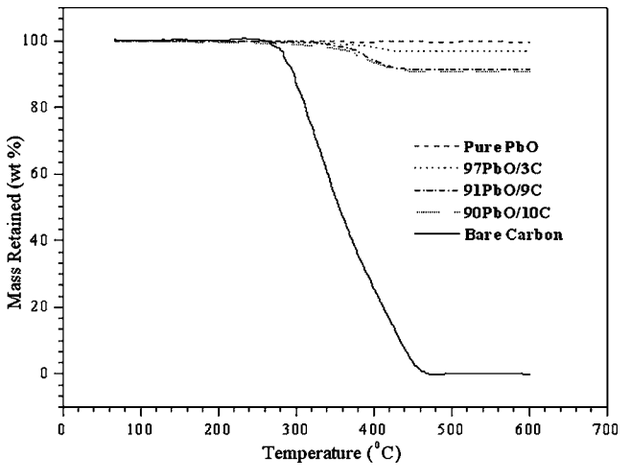

Figure 1. TGA curves of PbO-C nanocomposites with different PbO/C ratios.

Nova 1000 nitrogen gas analyzer using the Brunauer-Emmett-Teller (BET) method. Precise carbon contents in the PbO sprayed composites were determined by thermogravimetric and differential thermal analyses (TGA/DTA) via Setaram 92 equipment. Raman spectroscopy was used to monitor the variations in the carbon content using a JOBIN YVON HR800 confocal Raman system with 632.8 nm diode laser excitation on a 300 lines/mm grating at room temperature.

Electrode preparation and coin cells assembly.— The anode was prepared by mixing PbO, PbO-carbon composites, or spray pyrolyzed carbon as active materials with 10 wt % carbon black and 10 wt % polyvinylidene fluoride (PVDF) binder in *N*-methyl-2-pyrrolidinone (NMP) solvent to form a homogeneous slurry, which was then spread onto a copper foil. The coated electrodes were dried in a vacuum oven at 100°C for 24 h and then pressed. The electrochemical characterizations were carried out using coin cells. CR 2032 coin-type cells were assembled in an argon-filled glove box (Mbraun, Unilab, Germany) by stacking a porous polypropylene separator containing liquid electrolyte between the PbO electrode and a lithium foil counter electrode. The electrolyte used was 1 M $LiPF_6$ in a 50:50 (v/v) mixture of ethylene carbonate (EC) and dimethyl carbonate (DMC) provided by Merck KgaA, Germany.

Electrochemical measurements.— The cells were galvanostatically charged and discharged in the range of 0.01–1.50 V at a constant current density of 0.100 mA cm^{-2}. Cyclic voltammetry (CV) measurements were performed at a scanning rate of 0.1 mV s^{-1}. The ac impedance spectroscopy was obtained by applying a sine wave of 5 mV amplitude over a frequency range of 100.00 kHz to 0.01 Hz. Both the CV and ac impedance spectroscopy measurements were carried out using a CHI 660A electrochemical workstation system (CH Instrument, Cordova TN).

Results and Discussion

Estimation of the amount of carbon in the sprayed PbO-C nanocomposites.— For quantifying the amount of carbon in the PbO-C composite materials, TGA analysis was carried out in air. The samples were heated from 60 to 600°C at a rate of 5°C min^{-1}. Figure 1 shows the TGA analysis of the PbO-C composite samples along with those of bare PbO and carbon powders. As can be seen from Fig. 1, bare carbon powder burns off at 460°C, while the bare PbO powder remains stable in the temperature range used for this experiment. It can also be seen that the composites show weight loss at a temperature of 460°C, which corresponds to the oxidation of carbon. There is no further weight change in the composites after the initial oxidation of carbon. Therefore, the change in weight before and after the oxidation of carbon directly translates into the amount of carbon in the PbO-C composites. Using this method, it was found that the amounts of carbon in the composites are 3.3, 8.7, and 9.5 wt % for the precursor solutions with weight ratios [$Pb(NO_3)_2$/sugar] of 70/30, 40/60, and 15/85, respectively. Table I summarizes the actual carbon content in the spray pyrolyzed PbO-C nanocomposites. The carbon concentrations obtained after spray pyrolysis were significantly below the targeted levels. All samples undergo more than 80 wt % carbon losses during the spray process. This can be explained by the reactions during the spray pyrolysis process mentioned earlier.

Table I. Theoretical and actual carbon content in PbO-C nanocomposites sprayed from starting solutions with different concentrations of $Pb(NO_3)_2$/sugar.[a]

Starting solution wt % $Pb(NO_3)_2$/wt % sugar[a]	Theoretical weight % of carbon	Actual weight % of carbon (via TGA)	Mass loss % of carbon during spray pyrolysis
70/30	21.12	3.27	84.52
40/60	48.38	8.73	81.96
15/85	77.98	9.53	87.78

[a] $C_{12}H_{22}O_{11}$.

There are mainly three reactions during the spray pyrolysis process: (Eq. 1) oxidation of lead nitrate to produce lead oxide and release gases such as nitrogen dioxide and oxygen; (Eq. 2) decomposition of sugar to carbon and water vapor (in the absence of oxygen/air); and (Eq. 3) combustion of sugar in air to produce gases such as carbon dioxide and water vapor. All the reactions are exothermic and thus release excess energy produced during the reactions. As the spray pyrolysis process was carried out in air, reaction 3 is more favorable compared to reaction 2. Therefore, most of the sugar will be burnt out during the spray pyrolysis process, which accounts for the high percentage of carbon mass loss ($>$80 wt %). However, due to the instantaneous nature of the spray pyrolysis process, decomposition of sugar will still occur.[14,16] Equation 4 summarizes the whole reaction during the spray pyrolysis process.

Structure and morphology analysis of PbO-C nano composites.— X-ray diffraction investigations (Fig. 2) revealed

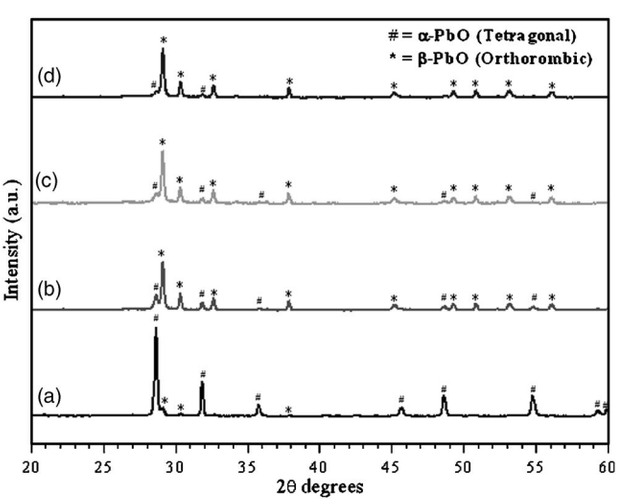

Figure 2. XRD patterns of PbO-C nanocomposites from (a) pure PbO; (b) 97PbO/3C; (c) 91PbO/9C; and (d) 90PbO/10C.

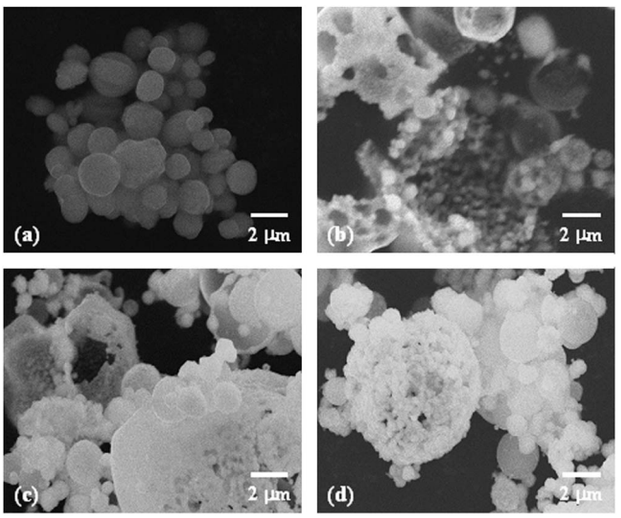

Figure 3. SEM images of PbO and PbO-C nanocomposites from (a) pure PbO; (b) 97PbO/3C; (c) 91PbO/9C; and (d) 90PbO/10C.

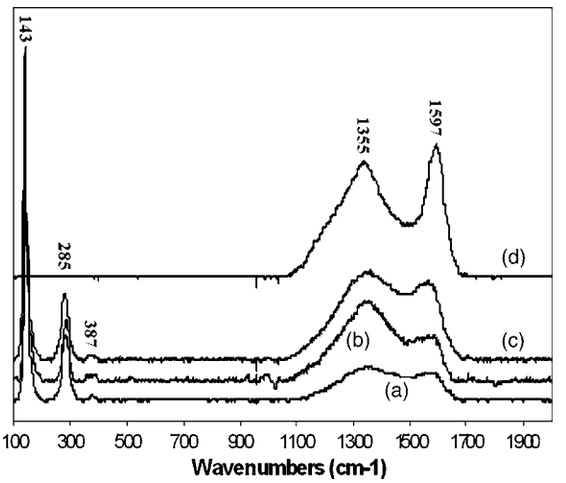

Figure 5. Raman spectra of PbO-C nanocomposites from (a) 97PbO/3C; (b) 91PbO/9C; and (c) 90PbO/10C; and (d) pure disordered carbon produced from sugar.

products comprising nanocrystalline PbO (Fig. 2a) and PbO-carbon nanocomposites (Fig. 2b-d with confirmation of both the α-PbO phase (ASTM 05-0561) and the β-PbO (ASTM 05-0570) phase. Figure 2 also reveals that as the carbon content increases (from Fig. 2a-d, the intensity of the orthorhombic β-PbO phase increases significantly while the intensity of the tetragonal α-PbO phase is reduced. The well-known Debye-Scherrer formula was used to estimate the approximate average crystal size using crystalline silicon as the reference material. The estimated average crystal size was reduced from 102 to 26 nm when the carbon content was increased. The reduction of the average crystal size led to an increase in specific surface area (S_{BET}) from 2.19 to 6.48 $m^2\ g^{-1}$. For comparison, the commercial Sigma-Aldrich PbO powders were only 0.42 $m^2\ g^{-1}$.

From SEM observations (Fig. 3), it was revealed that the particles are mainly spherical agglomerates, which is typical for the spray process, with sizes in the range of 0.2–2 μm for all powders. All the samples sprayed with sugar addition were morphologically alike, presenting a structure resembling broken hollow spheres with porosity on both the inside and the outside particle surfaces (Fig. 3b-d). This may be due to the decomposition of sugar, resulting in the release of gases such as carbon dioxide and water vapor, leaving holes in the hollow spherical structure.[14] Transmission electron microscopy (Fig. 4) confirmed the trend in average crystallite sizes as a function of carbon content, giving additional information about lead oxide morphology. The morphology of individual lead oxide crystallites in samples containing no carbon is shown in the TEM centered dark-field image (Fig. 4a), obtained using lead oxide diffraction spots. In the PbO-carbon samples, TEM combined with selected area electron diffraction (SAED) confirmed that the particle sizes ranged from 50–100 nm for the sample with 3 wt % carbon (Fig. 4b), and approximately 5–50 nm for the sample with 10 wt % carbon (Fig. 4c). Particles, such as those marked P in Fig. 4b, were found to be spheroidal or disklike in shape, while others were found to be slightly more faceted. Low-magnification bright-field imaging combined with SAED also confirmed that carbon-rich clusters formed during atomization, at least for the sample with 10 wt % carbon, and that these contained varying amounts of PbO. Some were solidified droplets containing no PbO nanoparticles at all (Fig. 4d), while many contained a uniform dense distribution of PbO such as that observed in Fig. 4c.

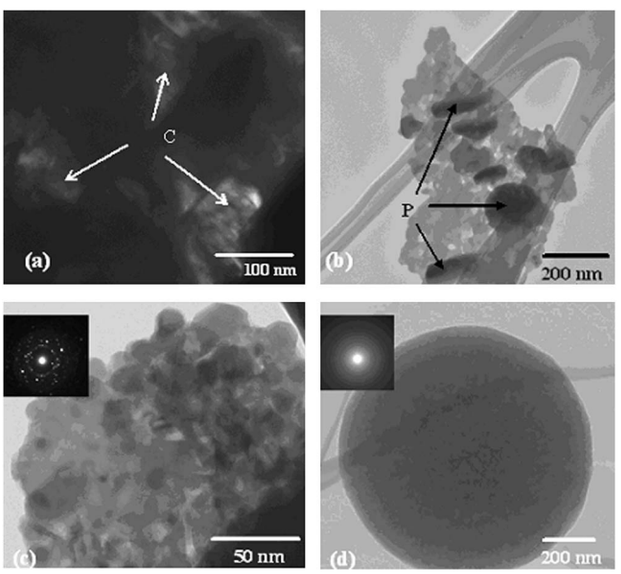

Figure 4. TEM images of PbO and PbO-C nanocomposites: (a) centered dark-field image of pure PbO, where individual crystallites are marked as *C*; (b) bright-field image of 97PbO/3C, with large PbO particles marked as P; (c) and (d) bright-field images and selected area electron diffraction patterns (inset) of 90PbO/10C. The lead oxide particles in the carbon rich cluster in (c) are significantly smaller than those in (b). Some carbon-rich clusters, such as that shown in (d), contained no lead oxide particles, as indicated by the diffuse contrast in the associated SAED pattern.

Table II. Physical properties of PbO-C nanocomposites.

Sample	Average crystal size, D_P (nm)	Specific surface area, S_{BET} ($m^2\ g^{-1}$)
Commercial PbO (Sigma-Aldrich)	>500	0.42
Pure PbO at 800°C, 0.5 M, and 3.14 mL min^{-1}	102	2.19
97PbO/3C	74	2.48
91PbO/9C	53	4.41
90PbO/10C	26	6.48

As a general trend, the increase in process temperature from the excess energy generated by the exothermic reactions in the Experimental section should have led to an increase in average crystal size due to the higher kinetics and intergrowth process. However, the results in Table II show otherwise. This can be explained by the phase transformation of α-PbO phase to β-PbO phase as the temperature increases. The excess energy generated by the spray pyrolysis process was used for the phase transformation process instead of crystal growth as the carbon content in the starting solution increased. This led to the reduction of crystal size and subsequently resulted in a higher specific surface area of the PbO-carbon nanocomposites.

Laser Raman spectroscopy gives information about the vibration of atoms in crystals and molecules and can be used as a complementary tool to XRD. Figure 5 presents Raman spectra of PbO-carbon nanocomposites obtained with 632.8 nm diode laser excitation on a 300 lines/mm grating at room temperature. The Raman spectrum of 97PbO/3C nanocomposite (Fig. 5a) displays two main peaks over 1000 cm^{-1} at around 1355 and 1597 cm^{-1}, which are designated as the D band and the G band[18] of disordered carbon, and another three peaks under 500 cm^{-1} which are due to the α/β-PbO (143 cm^{-1}) and the β-PbO (285 and 387 cm^{-1}).[19] This confirms that this kind of nanocomposite contains both PbO and disordered carbon (produced from spray pyrolysis of sugar). It also shows that the Raman intensity of disordered carbon increased with an increased percentage of sugar in the $Pb(NO_3)_2$/sugar raw material [see Raman spectra of PbO-C nanocomposites from (a) 97PbO/3C; (b) 91PbO/9C; and (c) 90PbO/10C; as well as (d) disordered carbon produced from sugar, respectively, in Fig. 5]. This indicates the increase of disordered carbon in the PbO-C nanocomposites. This result is in good agreement with results obtained by both the XRD and TGA methods.

Energy dispersive X-ray (EDX) mapping of different elements (C and Pb) was conducted to investigate the distribution of the species within the agglomerated particles (Fig. 6). The bright spots correspond to the presence of each element. Based on the EDX elemental maps of PbO–C nanocomposites from 90PbO/10C (left) and 97PbO/3C (right), respectively, in Fig. 6, distribution of carbon in the PbO-carbon nanocomposites is, within the limits of SEM-

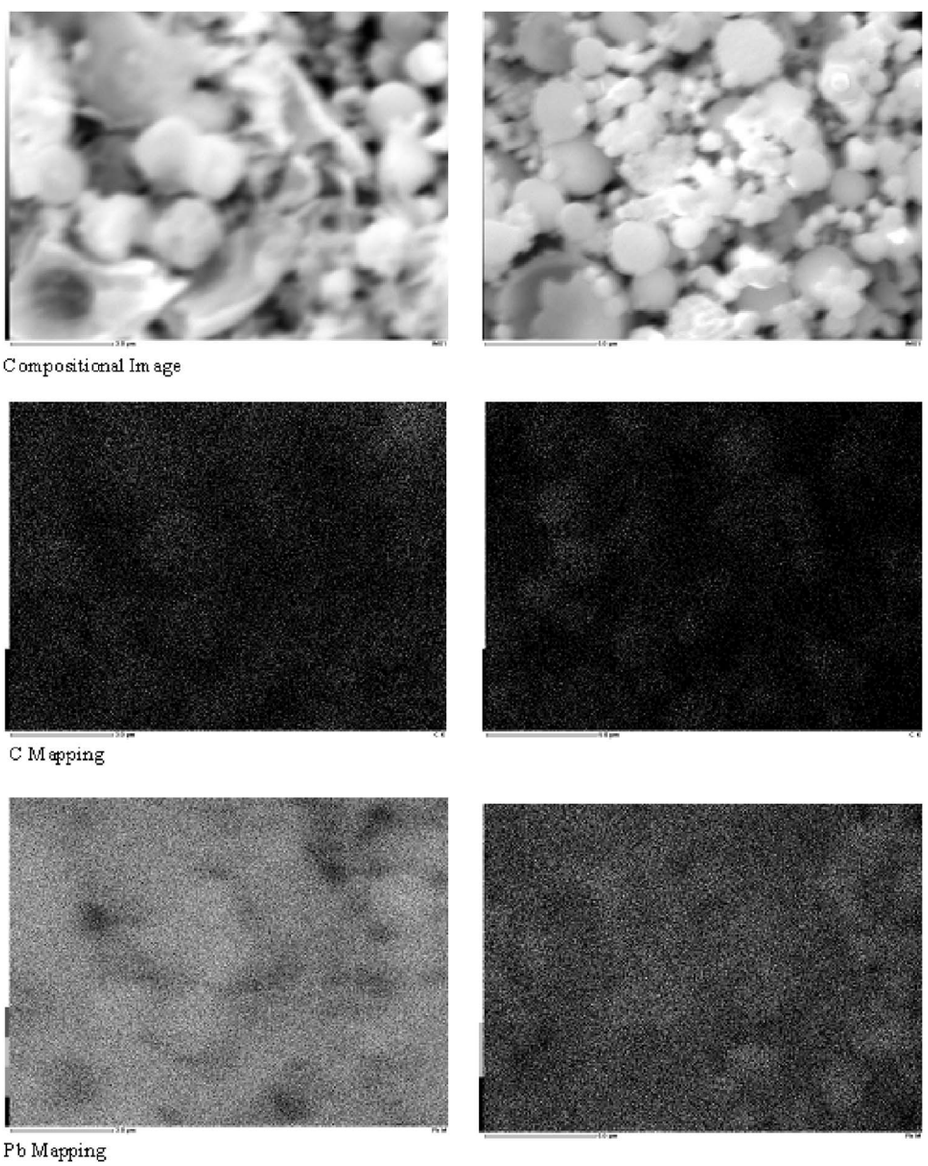

Figure 6. EDX mapping of PbO-C nanocomposites made from 90PbO/10C (left) and 97PbO/3C (right).

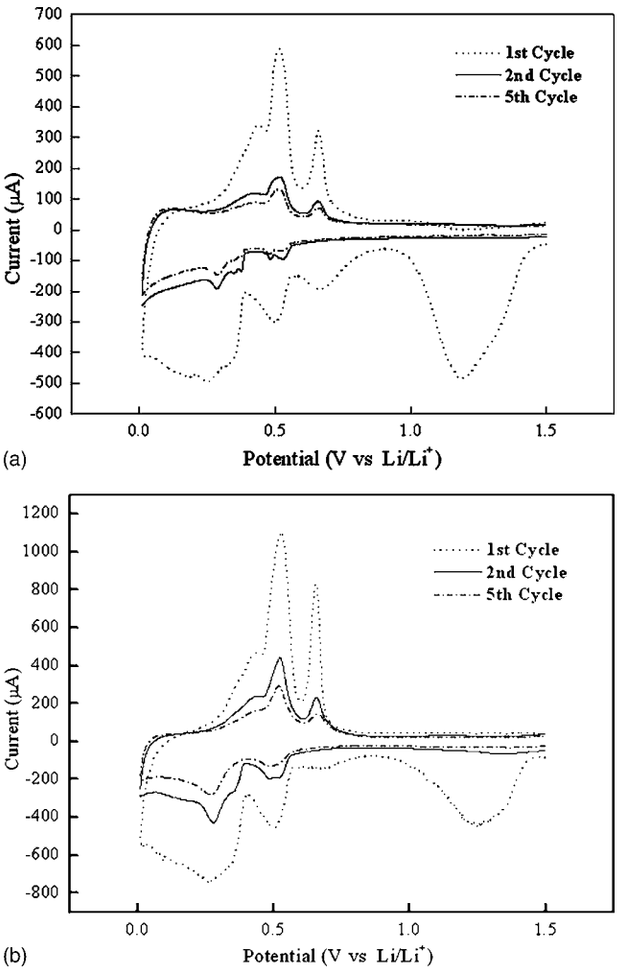

Figure 7. CVs of PbO-C nanocomposites from (a) pure PbO and (b) 90PbO/10C. The scan rate was 0.1 mV s^{-1}.

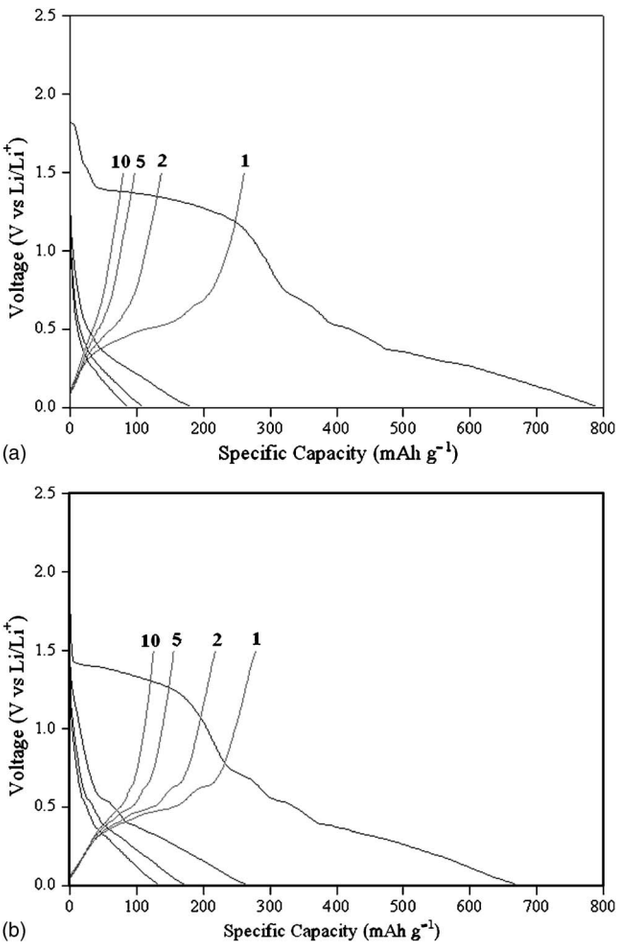

Figure 8. The first, second, fifth, and tenth charge/discharge profiles of PbO-C nanocomposites from (a) pure PbO and (b) 90PbO/10C. The current density was 0.100 mA cm^{-2}.

EDS resolution, apparently homogeneous, regardless of the carbon content in the samples. This indicates that a uniform distribution of carbon on all PbO particles can be achieved by spray pyrolyzing a sugar solution.

Electrochemical performance of PbO-C nanocomposites.— Cyclic voltammograms (CVs) of nanocrystalline PbO (Fig. 7a) and 90PbO/10C (Fig. 7b) nanocomposite electrodes in lithium-ion coin cells, in which a lithium foil was used as the counter electrode and reference electrode, are shown in Fig. 7. The coin cells were cycled at a scan rate of 0.1 mV s^{-1}. The CV curves for both the nanocrystalline PbO and for the electrodes with 10 wt % carbon clearly indicate the irreversible reactions during the first discharge with two reduction peaks, one between 1.45 and 0.9 V and another at 0.7 V. The peak between 1.45 and 0.9 V can be assigned to the replacement reaction converting PbO to Pb with the formation of Li_2O. According to Martos et al.,[9,15] this transformation of Pb(II) $\rightarrow$ Pb(0) takes place through some intermediates, i.e., Pb (I). Meanwhile, the reduction peak at 0.7 V can be ascribed to the formation of the solid electrolyte interface (SEI) layers, which only happens in the first discharge cycle.[20-22] The low potential region ($<$0.7 V) exhibits several peaks corresponding to the formation of Li_xPb alloys. Huggins[4,5] identified four potential plateaus at 0.601, 0.449, 0.374, and 0.292 V over the composition range $0 < x < 4.5$ (i.e., LiPb, $Li_{3.0}Pb$, $Li_{3.2}Pb$, and $Li_{4.5}Pb$). In the first discharge for both the nanocrystalline PbO and 90PbO/10C nanocomposite electrodes, three cathodic peaks were found at 0.50, 0.38 (weak), and 0.28 V, which are slightly different from the values reported by Huggins.[4,5] Subsequent charging and discharging of both the nanocrystalline PbO and 90PbO/10C nanocomposite electrodes show that the potential peaks of the anodic and cathodic waves correspond better to the lithium-lead alloys formed according to Huggins.[4,5]

A large volume change occurs in the Pb region during lithium insertion and extraction reactions. Consequently, the mechanical stress and aggregation of particles leads to the cracking and crumbling of the electrodes. As a result, electrical contacts between particles are lost and cause a sharp decrease in specific capacity and cycle life of the electrodes. The specific capacity and cycling stability of the nanocrystalline PbO and PbO-carbon nanocomposite electrodes were measured by constant current charging/discharging at 0.100 mA cm^{-2} between 0.01 and 1.50 V. Figure 8 shows the first, second, fifth, and tenth charge/discharge curves of the nanocrystalline PbO (Fig. 8a) and 90PbO/10C (Fig. 8b) nanocomposite electrodes. The discharge curves of nanocrystalline PbO and 90PbO/10C nanocomposite are fairly similar in appearance. In addition, irreversible capacity losses during the first cycle were 611 and 405 mAh g^{-1} for pure PbO and 90PbO/10C nanocomposite, respectively. The irreversible capacity loss decrease with increased carbon content was due to the presence of the carbon matrix, which is a good electronic conductor and provides an effective cushion for volume expansion.[14,16,17] Furthermore, the reversibility of the

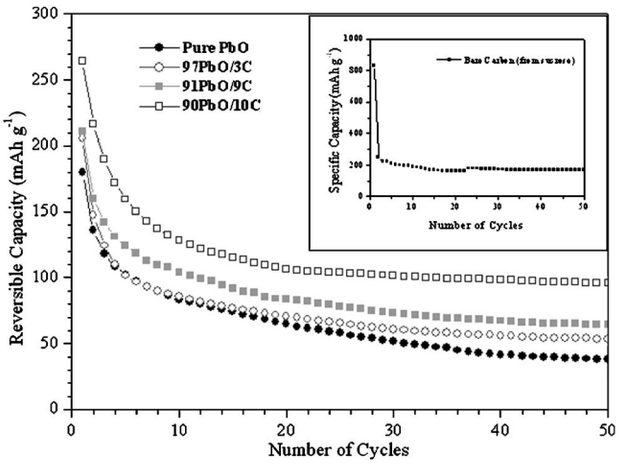

Figure 9. Cycle life of PbO-C nanocomposites. The current density was 0.100 mA cm^{-2}. The inset figure presents the specific capacity *vs* cycle number data for the bare carbon powder and the current density applied was also 0.100 mA cm^{-2}.

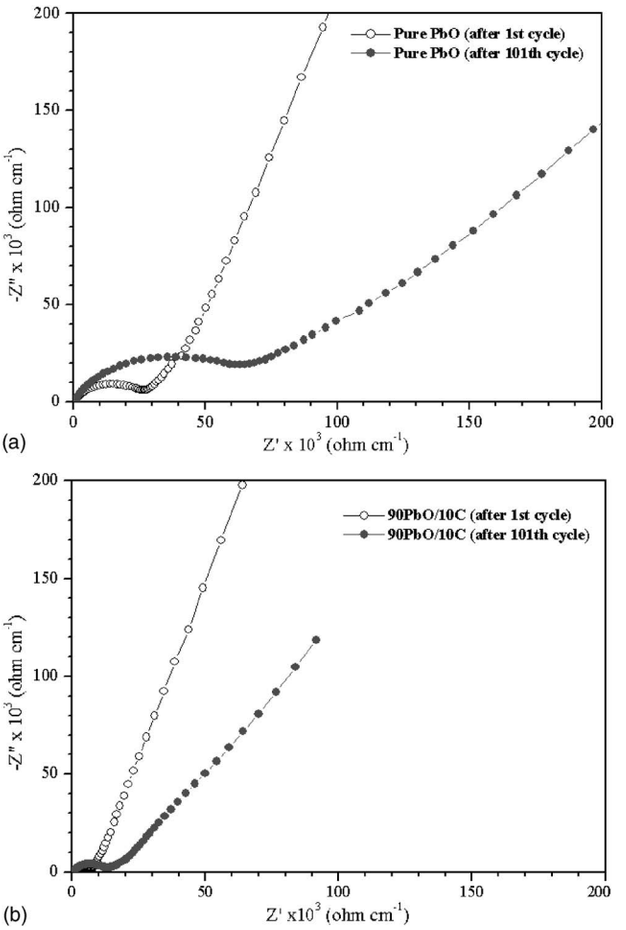

Figure 10. Impedance plots for (a) pure PbO and (b) 90PbO/10C electrodes in the delithiated state.

90PbO/10C nanocomposite electrodes was better than that of the nanocrystalline PbO electrodes, as indicated by the retention of the potential plateaus after ten cycles.

The reversible capacities as a function of cycle number are compared in Fig. 9. Initial reversible capacity is as high as 265 mAh g^{-1} for the 90PbO/10C nanocomposite electrodes. Subsequently, the reversible capacity was maintained above 100 mAh g^{-1} beyond 50 cycles for the 90PbO/10C nanocomposite electrodes, which is higher than the values reported by Martos et al.[9] for lead oxide powder anodes in lithium-ion rechargeable batteries. This shows that PbO-carbon nanocomposites are promising as anode materials for Li-ion batteries. Meanwhile, the spray pyrolyzed carbon powder (from sucrose solution) was found to have a capacity of 170 mAh g^{-1} after 50 cycles, as shown in the inset of Fig. 9. This means that the spray pyrolyzed carbon in the composite materials, which is considered as an active material in this study, contributed only 17 mAh g^{-1} for the 90PbO/10C nanocomposite, which accounted for 17% of its total reversible capacity (100 mAh g^{-1}). In addition, we also found that the cycle life increases with increasing carbon content in the nanocomposites. For example, the reversible capacity efficiency ($R_{\text{cycle number}}/R_{\text{1st cycle}}$) for 90PbO/10C nanocomposite electrodes after 50 cycles is 36.3% compared to 21.1% for nanocrystalline PbO electrodes.

We believe that the nanostructure of the spray pyrolyzed powder and the conductivity and ductility of the carbon matrix are responsible for the good cyclability of the PbO-carbon nanocomposites. To verify the effect of carbon content on the electronic conductivity of the nanocomposites, ac impedance measurements were conducted. The Nyquist plots obtained for the nanocrystalline PbO (Fig. 10a) and 90PbO/10C (Fig. 10b) nanocomposite electrodes after 1 and 101 cycles are compared in Fig. 10. The thickness of the electrodes was controlled at 50 μm and the coated area of the electrodes at 1 cm^2. To maintain uniformity, electrochemical impedance spectroscopy (EIS) experiments were performed on working electrodes in the fully charged state. In general, one semicircle in the high-frequency range was observed for all samples. The diameter of the semicircle represents the interparticle contact resistance.[23] Meanwhile, in the low-frequency region, an angled straight line was obtained which represents a diffusion-controlled process in the solid electrolyte interface.[24] In addition, we found that the diameter of the semicircles was enlarged after 101 cycles for all the samples. However, when Fig. 10a is compared to Fig. 10b, considerable differences are observed. The diameter of the semicircle after 101 cycles increased by more than 40 000 ohms cm^{-1} in the case of nanocrystalline PbO electrodes compared to 6000 ohms cm^{-1} for 90PbO/10C nanocomposite electrodes. Therefore, it can be assumed that the interparticle resistance was suppressed with the addition of carbon, resulting in better cycling of the cells during the charge/discharge process.[23]

Conclusions

A series of PbO-carbon nanocomposites has been synthesized via in situ spray pyrolysis of $Pb(NO_3)_2$/sugar solution at 800°C and a flow rate of 3.14 mL min^{-1}. The spray pyrolyzed powders are fine nanocrystalline PbO homogeneously distributed within an amorphous carbon matrix with highly developed surface area. Both the XRD patterns and TEM images revealed that the PbO-carbon nanocomposite crystal sizes were approximately 26–102 nm. The carbon content estimated by TGA shows that a huge amount of carbon mass (>80 wt %) was lost during the spray pyrolysis process. Raman spectroscopy also revealed increases in the amount of disordered carbon (from the pyrolyzed sugar solution) with increasing sugar content in the starting solution. The distribution of carbon in the sprayed samples was homogeneous, as revealed by the elemental EDX mapping. The alloying and dealloying of lithium with lead over the 1.50 to 0.01 V range yields various Li_xPb ($x < 4.5$) alloys. The PbO-carbon nanocomposites showed an improved cycle life as the carbon content increased. We strongly believed that the presence of the carbon matrix, which is a good electric conductor, provides an effective cushion to absorb volume change during the alloying and dealloying processes within the lead region.

Acknowledgments

Financial support provided by the Australian Research Council (ARC) through the ARC-Linkage project (LP0219309) and the ARC Centre of Excellence funding (CE0348245) is gratefully acknowledged. Many thanks also go to S. Bewlay, R. Kinnell, L. Zhao, and Z. J. Lao for their assistance in the spray pyrolysis process. Finally, the authors also thank Dr. T. Silver for a critical reading of the manuscript.

University of Wollongong assisted in meeting the publication costs of this article.

References

1. Y. Idota, M. Mishima, Y. Miyaki, T. Kubota, and T. Miyasaki, Canadian Pat. Appl., 2,134,052 (1994).
2. Y. Idota and M. Mishima, Canadian Pat. Appl., 2,143,388 (1995).
3. J. Wang, I. D. Raistrick, and R. A. Huggins, *J. Electrochem. Soc.*, **133**, 457 (1986).
4. R. A. Huggins, *J. Power Sources*, **26**, 109 (1989).
5. R. A. Huggins, *Solid State Ionics*, **113–115**, 57 (1998).
6. H. Li, X. Huang, and L. Chen, *Solid State Ionics*, **123**, 189 (1999).
7. J. Yang, M. Winter, and J. O. Besenhard, *Solid State Ionics*, **90**, 281 (1996).
8. P. Poizot, S. Laurelle, S. Grugeon, L. Dupont, and J. M. Tarascon, *Nature (London)*, **407**, 496 (2000).
9. M. Martos, J. Morales, L. Sanchez, R. Ayouchi, D. Leinen, F. Martin, and J. R. Ramos Barrado, *Electrochim. Acta*, **46**, 2939 (2001).
10. M. Cruz, L. Hernan, J. Morales, and L. Sanchez, *J. Power Sources*, **108**, 35 (2002).
11. J. O. Besenhard, M. Hess, and P. Komenda, *Solid State Ionics*, **40/41**, 525 (1990).
12. R. A. Huggins, *J. Power Sources*, **81–82**, 13 (1999).
13. K. Konstantinov, J. Wang, S. Bewlay, G. X. Wang, H. K. Liu, S. X. Dou, and J. H. Ahn, *J. Metastable Nanocryst. Mater.*, **15–16**, 325 (2003).
14. L. Yuan, K. Konstantinov, G. X. Wang, H. K. Liu, and S. X. Dou, *J. Power Sources*, **146**, 180 (2005).
15. M. Martos, J. Morales, and L. Sanchez, *Electrochim. Acta*, **48**, 615 (2003).
16. S. L. Bewlay, K. Konstantinov, G. X. Wang, S. X. Dou, and H. K. Liu, *Mater. Lett.*, **58**, 1788 (2004).
17. M. Yoshio, H. Wang, K. Fukuda, T. Umeno, N. Dimov, and Z. Ogumi, *J. Electrochem. Soc.*, **149**, A1598 (2002).
18. M. Yoshikawa, G. Katagiri, H. Ishida, and A. Ishitani, *Solid State Commun.*, **66**, 1177 (1988).
19. D. U. Wiechert, S. P. Grabowski, and M. Simon, *Thin Solid Films*, **484**, 73 (2005).
20. T. Wang, Z. Ma, F. Xu, and Z. Jiang, *Electrochem. Commun.* **5**, 599 (2003).
21. Q. Pan, K. Guo, L. Wang, and S. Fang, *J. Mater. Chem.*, **12**, 1833 (2002).
22. K. Naoi, N. Ogihara, Y. Igarashi, A. Kamakura, Y. Kusachi, and K. Utsugi, *J. Electrochem. Soc.*, **152**, A1047 (2005).
23. J. Fan and P. S. Fedkiw, *J. Power Sources*, **72**, 165 (1998).
24. H. Li, X. Huang, and L. Chen, *J. Power Sources*, **81–82**, 340 (1999).